Preliminary Design and Performance Analysis of the Liquid Turbine for Supercritical Compressed Air Energy Storage Systems

Hongyang Li
E-mail: lihongyang0@126.com
Institute of Engineering Thermophysics, Chinese Academy of Sciences
University of Chinese Academy of Sciences

Ziyi Shao
E-mail: shaoziyi@iet.cn
Institute of Engineering Thermophysics, Chinese Academy of Sciences
University of Chinese Academy of Sciences

Xuehui Zhang
E-mail: zhangxuehui@iet.cn
Institute of Engineering Thermophysics, Chinese Academy of Sciences

Yangli Zhu
E-mail: zhuyangli@iet.cn
Institute of Engineering Thermophysics, Chinese Academy of Sciences

Wen Li
E-mail: liwen@iet.cn
Institute of Engineering Thermophysics, Chinese Academy of Sciences
University of Chinese Academy of Sciences

Haisheng Chen[1]
E-mail: chen_hs@mail.etp.ac.cn
Institute of Engineering Thermophysics, Chinese Academy of Science
University of Chinese Academy of Sciences
National Energy Large Scale Physical Energy Storage Technologies R&D Center of Bijie High-tech Industrial Development Zone

Zhibin Yu
E-mail: Zhibin.Yu@glasgow.ac.uk
James Watt School of Engineering, University of Glasgow

Abstract

Liquid turbines can replace throttling valves to recover waste energy and reduce vaporization in various industrial systems, such as liquefied natural gas, air separation, supercritical compressed

[1] Corresponding author.

air energy storage (SC-CAES) systems, et al. However, there were few studies about differences in the preliminary design method between general radial inflow turbines and liquid turbines. In this paper, a preliminary design method of liquid turbines was presented, and the performance of liquid turbines was predicted using CFD methods which were validated with experimental results. The efficiency of the designed liquid turbine was 92% and the output power was 65.7 kW. The performance of the turbine predicted by the preliminary method could agree with simulation results of prototype and model turbines near the design working condition, while there was a certain deviation when the flow rate was less than 70%. Through analyzing the presented preliminary design method, it could be found that distinctive differences in thermal properties of working fluids caused that typical design parameters for liquid turbines, like ratios of the blade height, the hub radius and the area, should be selected differently from empirical values for gas radial turbines. The results obtained in this paper could help guide the design of liquid turbines for various systems to promote energy conservation and improve system efficiencies significantly.

Keywords: Liquid turbine; SC-CAES; Throttling valves; Radial inflow turbine; Preliminary design method

1 Introduction

Throttling valves are extensively equipped to depressurize the flow in various industrial systems. However, a certain amount of the internal energy is dissipated in the isenthalpic depressurization process and a large fraction of the liquid is vaporized and wasted when the pressure is lower than the saturation pressure. Replacing throating valves with liquid turbines can improve the system performance due to the recovery of the internal energy and the alleviation of the vaporization in many traditional systems [1], such as liquefied natural gas and air separation systems. The liquid turbine studied in this paper is applied in the supercritical compressed air energy storage (SC-CAES) system, which can balance the load and eliminate the dependence on fossil fuel and cavern using compressors, expanders, heat exchangers, liquid turbines, cryogenic storage tank and cryopump [2,3]. Compared with other compressed air energy storage (CAES) systems, the benefit of using the liquid turbine in the SC-CAES system is more evident because the system efficiency can be increased by about 10% [2,4,5].

The liquid turbine is a kind of turbomachinery designed for recovering waste energy of the liquid or supercritical fluid in traditional throttling processes, and a type of energy recovery expanders [6,7] which includes the positive displacement expander and the liquid turbine. The positive displacement expander was extensively studied in the past because it could be conveniently modified for the expansion process from positive displacement compressors. Taniguchi et al. [8] studied analytically and experimentally a two-phase screw expander which was applied to produce power for refrigeration or heat pump cycles. Kliem [9] tested a screw expander with saturated water as the inflow and the maximum efficiency was 56% in the experiment. Other researchers also investigated the performance of the screw expander under various fluids, such as R113 [10] and R134a [11]. Vasuthevan and Brümmer [12] and Bianchi et al. [13] modelled the two-phase flow in the twin screw expander for trilateral flash cycle numerically. Kakuda et al. [14] tested a coupled scroll type expander and compressor for CO_2 refrigeration cycle. Wang et al. [15] designed a compliant scroll expander which allowed for the liquid flashing. Xia et al. [16] studied experimentally a vane expander using R410A as the working fluid and suggested that the maximum

COP of the refrigeration system with their optimized vane expander could be improved by 8.97% than the system with the throttling valve. Ferrara et al. [17] measured the performance of a radial piston expander for a CO_2 refrigeration system and concluded that the COP of the system could be improved by 7.4%. Galoppi et al. [18] tested the radial piston expander for a heat pump with the R134a as the working fluid. Nickl el al. [19] studied a three-stage expander for replacing the throttle valve in a CO_2 refrigeration system.

Liquid turbines can be applied in various industrial systems and classified into several types [20]. Wang et al. [21] carried out experimental and numerical investigation on the cryogenic liquid turbine for air separation and LNG production systems. The maximum total efficiency of the radial inflow liquid turbine was 74.8%. Li et al. [22], Song et al. [23,24], He et al. [25] and Sun et al. [26] studied numerically the cavitation behaviour of the liquid turbine. Ren et al. [27] studied the strength of the impeller, while Wang et al. [28] predicted the axial thrust loading on the impeller. Song et al. [29] presented an optimization design method for the liquid turbine. Li et al. [30,31] also studied experimentally and numerically a liquid turbine for the SC-CAES system and the maximum efficiency was 75%. The radial inflow turbine has been a major type of liquid turbine for cryogenic applications, such as air separation [32] and liquefied natural gas [21] and SC-CAES systems [30]. The radial inflow turbine has benefits in ruggedness, shaft power per stage and manufacture [33] and has been widely applied as energy output devices, such as gas turbines [34], turbochargers [35] and power-producing machines in organic Rankine cycles [36–38] and other systems [39,40]. Design and optimization methods of general radial inflow turbines have been extensively studied for water [41], gas [33,42–46], air [47,48], refrigerant [49–51] and CO_2 [52,53] applications.

However, general design methods for gas radial turbines cannot be directly used for liquid turbines. Firstly, the ideal gas state equation or real gas equation brings large errors and high uncertainty when deriving the performance of the liquid turbine. Secondly, mathematical models in general preliminary design methods should be altered for the fluids in the liquid turbine. Thirdly, ranges of empirical parameters for general radial inflow turbines may be not suitable and should be modified for the liquid turbine. Fourthly, conventional design methods of water turbines can not be applied to liquid turbines directly because most liquid turbines have low specific speeds due to low flow rates and high rotational speeds, and working fluids of liquid turbines should be sealed properly to prevent from being mixed with other fluids, including air, oil and so on.

The preliminary design method for liquid turbines has not been presented and its differences from the method for general gas turbines has not been discussed in previous research. The designed liquid turbine using conventional design methods and empirical parameters of gas radial turbines may not meet requirements of the structure and the strength. Therefore, the special design method of liquid turbines is of high importance to their applications in industrial systems.

In this paper, the preliminary design method and model test model are proposed for liquid turbines in SC-CAES systems. The liquid turbine is designed, while the performance of the liquid turbine is investigated numerically and experimentally. Section 2 describes mathematical models for correlating geometrical and flow parameters. Section 3 illustrates the design procedure and model test method. The experimental and numerical performance of the liquid turbine is presented in Section 4. Ranges of geometrical parameters are discussed in Section 5.

2 Thermal, geometrical and mathematical models

2.1 Thermal processes

The SC-CAES system [5] is a flexible and large-scale mechanical energy storage method. It can use compressors and heat exchangers to pressurize and cool the air to the supercritical state when the electrical load is low. When the power supply is insufficient, this energy storage system can generate and supply the electricity using generators and expanders, which can transform the internal energy of the supercritical air to the shaft power of turbines. During the energy storage process, the outflow of the cooler is high-pressure liquid air. For safety and other reasons, the liquid in the tank has a low pressure. To depressurize the fluid, the throttling valve has to be used in the system during the energy storage process. However, the deployment of the throttling valve creates much exergy loss and decreases the efficiency of the system.

The liquid turbine can be used in the system to replace the throttling valve, as shown in Figure 1(a). Thus, the deduction of the internal energy of the air can be recovered by the liquid turbine, while the vaporization of the fluid during the depressurization process can be reduced. The liquid turbine can significantly enhance the efficiency of the stem during the energy storage process. Guo et al. [2,5] has discussed the benefit of utilization of the liquid turbine for the SC-CAES system in detail.

Although advantages of using liquid turbines have been clarified in previous research, the design and manufacture of liquid turbines for the SC-CAES system have not been understanded sufficiently. The flow process inside liquid turbines is quite different from that of general radial turbines and water turbines, as shown in Figure 1(b). A_0 is the state at the inlet of a liquid turbine, A_1 is the state at the outlet of the nozzle of the liquid turbine, and A_3 is the state at the outlet of the liquid turbine. It can be found that the reduction of the temperature is much lower than that of gas radial turbines, the fluid state is liquid and gas state equations are not suitable for deriving performance of the liquid turbine. Therefore, it can be implied that conventional design methods of gas radial turbines can not be used for designing liquid turbines.

The two-phase turbine [54,55] can also be used in the SC-CAES system. The inflow of the two-phase turbine is in the liquid state, and the outflow is two-phase mixture. Thus, it not only recovers the energy of the liquid, but also the gas-liquid mixture. Ideally, two-phase turbines are more suited to the SC-CAES system than liquid turbines. However, the efficiency of two-phase turbines is much lower than liquid turbines in the current research. The enhancement of two-phase turbines needs further investigation. Thus, the utilization of liquid turbines is more practical for the SC-CAES system, and the development of liquid turbines is feasible based on experiences of designing gas radial turbines and water turbines.

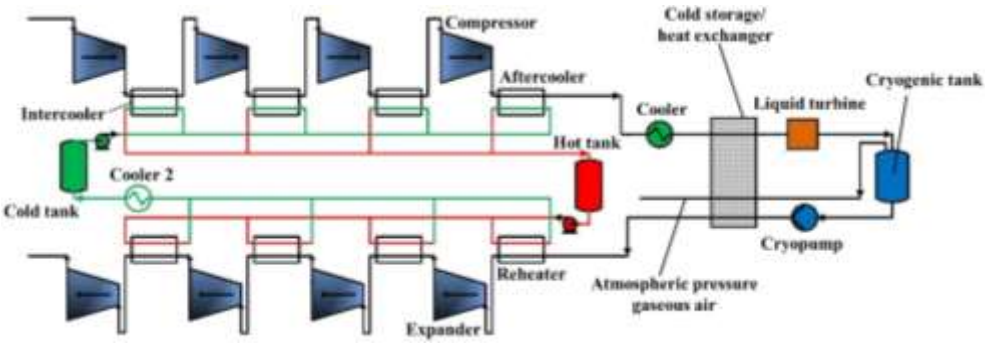

(a) Diagram of the SC-CAES system[2]

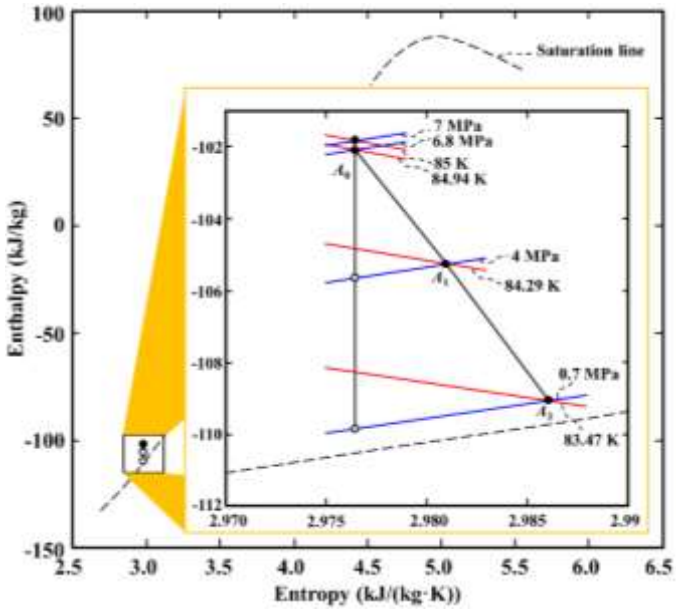

(b) Enthalpy-entropy diagram for the liquid turbine

Figure 1 Diagram of the SC-CAES and processes in the liquid turbine

2.2 Geometrical model

During the preliminary design process for the liquid turbine, geometries of the nozzle and the rotor are designed and optimized to make the performance of the turbine as high as possible, as shown in Figure 2(a). The passage is often projected and modelled in a meridian plane, and computational stations are defined as illustrated in Figure 2(b). The inlet of the nozzle is at Station 0. The outlet of the nozzle is at Station 1. The inlet of the rotor is at Station 2. The outlet of the rotor is at Station 3. Each station has two control nodes, which represents the hub and the shroud separately.

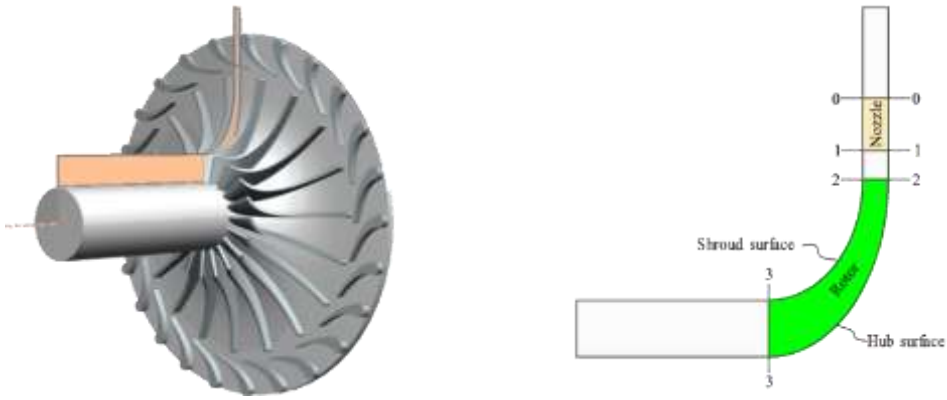

(a) Nozzle and rotor in three-dimension (b) Nozzle and rotor in the meridional plane

Figure 2 Structure of the liquid turbine

Flow parameters include relative velocity, absolute velocity, relative flow angle, absolute flow angle, pressure, and so on. Geometrical parameters include positions of nodes, blade angle, height of blades, blade numbers, and so on. Thus, for a computational station, the set of all parameters is

$$X_j\left(C_r, C_u, C_m, W_r, W_u, W_m, \alpha, \beta, p, r, Z, \theta, \mathrm{K}\right) \tag{1}$$

However, due to lacking practices of liquid turbines, effects of seals and gaps on the performance of liquid turbines are not clear. Thus, during the preliminary design, the deduction of the

performance caused by seals and gaps is not considered in this paper.

2.3 Mathematical models

For a general radial inflow turbine, several dimensionless parameters can be defined, such as reaction ratio Ω, speed ratio $\bar{u}$, rotor radius ratio $\bar{D}$, velocity ratio σ, loading coefficient Ψ, flow rate, coefficient Φ, and so on [45]. These dimensionless parameters are not independent and have separate physical concepts. Mathematical methods for gas turbines cannot be directly used to design liquid turbines. For example, if the working fluid is the liquid nitrogen at the inlet temperature 85 K and the inlet pressure 7.0 MPa, state points at the inlet of the nozzle and rotor can be illustrated in Figure 2(b), as well as the state point at the outlet of the rotor. It can be found that all state points are located in the subcooling zone, and the process line approaches the saturated liquid line. Both the inflow and the outflow of the designed liquid turbine are subcooled liquid nitrogen. All state points are close to each other, and the line of the isentropic process is close to that of the real process in the enthalpy-entropy diagram of the nitrogen. The variation of the fluid's temperature in the liquid turbine is within 1 K. Considering measurement accuracy and inhomogeneity of the flow, design errors will be significant when design methods of gas turbines are applied for liquid turbines.

Bernoulli's equation, as illustrated in Equation (2), can be used in liquid turbines under a series of assumptions, including steady and rotational flow, potential mass force and barotropic fluid. If the total pressure of the fluid is constant, the ideal velocity at rotor outlet C_0 is $\sqrt{2\,(p_0^0 - p_3)/\rho}$.

$$Z_h + \frac{p}{\rho g} + \frac{C^2}{2g} = \text{Const} \tag{2}$$

In a relative coordinate, Bernoulli's equation can be changed to Equation (3) if the variation of the altitude is neglected.

$$\frac{p}{\rho g} + \frac{W^2 - U^2}{2g} = \text{Const}_{rel} \tag{3}$$

For the nozzle, the nozzle efficiency η_N can be defined as

$$\eta_N = \frac{C_2^2}{2\left(p_0^0 - p_2\right)/\rho} \tag{4}$$

From Equation (4), the total pressure loss in the nozzle can be deduced as

$$\Delta p_N = \frac{\rho C_2^2}{2}\frac{1-\eta_N}{\eta_N} \tag{5}$$

If the variation of the fluid's density is small, the reaction degree Ω can be read as

$$\Omega \cong \frac{p_2 - p_3}{p_0^0 - p_3} \tag{6}$$

The speed ratio $\bar{u}$, which is related directly to the turbine efficiency, is derived in Equation (7). For a large Ψ, the speed ratio $\bar{u}$ increases rapidly as β_2 decreases. If β_2 is very small, the magnitude of the increment is relatively low.

$$\bar{u} = \sqrt{\frac{(1-\Omega)\eta_N}{\Psi^2 + \cot^2\beta_2\left(1-\Psi\right)^2}} \tag{7}$$

Based on Euler equation, the turbine efficiency is defined as Equation (8) without the leakage, friction and mechanical losses included.

$$\eta_u = \frac{2\left(C_{u2}U_2 - C_{u3}U_3\right)}{C_0^2} \tag{8}$$

If parameters of the loading coefficient Ψ, flow coefficient Φ, velocity ratio $\bar{u}$ and absolute flow angle α_3 are given, the circumferential velocity at the inlet of the rotor C_{u2} is ΨU_2, the axial velocity at the outlet of the rotor C_{m3} is ΦU_2, and the blade velocity at the outlet of the rotor U_3 is $\bar{D}U_2$. Velocity triangles at the inlet and outlet of the rotor are shown in Figure 3. In this paper, the flow angle is positive when the direction of circumferential velocity is the same as the rotational direction.

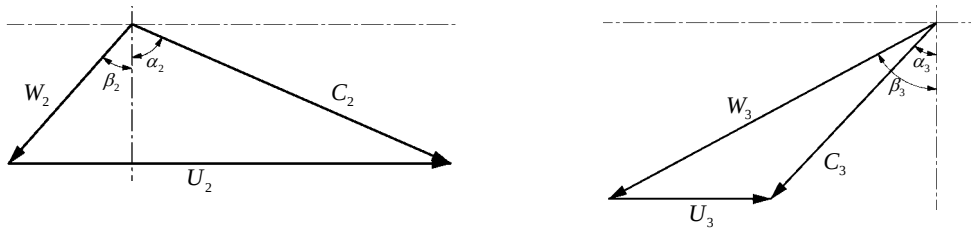

(a) Rotor inlet (b) Rotor outlet

Figure 3 Velocity triangles at the inlet and outlet of the rotor

Using conversation equations and geometrical relationships, typical geometrical parameters can be derived and summarized in Table 1. The efficiency of a liquid turbine is

$$\eta = 2\bar{u}^2\left(\Psi + \bar{D}\Phi\tan\alpha_3\right) \tag{9}$$

The absolute flow angle α_2 at the inlet of the rotor is

$$\alpha_2 = \arctan\left(\frac{\Psi\tan\beta_2}{\Psi - 1}\right) \tag{10}$$

The absolute flow angle β_3 at the outlet of the rotor is

$$\beta_3 = \arccos\left[\frac{\Phi\sin\beta_2}{\sigma\left(\Psi - 1\right)}\right] \tag{11}$$

Table 1 Expression of dimensionless parameters

Parameter	Expression	
Radius ratio of the impeller between the outlet and inlet of the rotor $\bar{D}$	$\bar{D} = \sqrt{\frac{\sigma^2\left(1-\Psi\right)^2}{\sin^2\beta_2} - \Phi^2} - \Phi\tan\alpha_3$	(12)
Height ratio of the blade at the inlet of the rotor $\bar{h}_2$	$\bar{h}_2 = \frac{\pi\tan\beta_2}{3600\sqrt{2}\left(\Psi-1\right)\bar{u}^3}\frac{n_q^2}{g^{1.5}}$	(13)
Height ratio of the blade at the outlet of the rotor $\bar{h}_3$	$\bar{h}_3 = \frac{\pi}{3600\sqrt{2}}\frac{1}{\bar{u}^3\Phi\bar{D}}\frac{n_q^2}{g^{1.5}}$	(14)
Area ratio of the flow passage between the inlet and outlet of the rotor $\bar{A}$	$\bar{A} = \frac{\Psi - 1}{\Phi\tan\beta_2}$	(15)

Figure 4 shows the variation of the efficiency with Ψ, Φ and α_3 using the above relationship when $\bar{u}$ is 0.7 and σ is 1.3. The efficiency of the liquid turbine increases as the loading coefficient increases and the flow coefficient decreases. It can be found that when α_3 is negative, contours of

the efficiency are upwards convex; when α_3 is positive, the contours are upwards concave; and when α_3 is equal to zero, the contours are in the horizontal direction and the efficiency could be simplified to $2\bar{u}^2\Psi$. The three situations for α_3 represent different conditions for the rotor. It indicates that a negative α_3 is beneficial for a higher turbine efficiency, but α_3 cannot be as low as possible due to limitations from the structure. Thus, compromises have to be made to meet structure requirements and enhance the turbine efficiency.

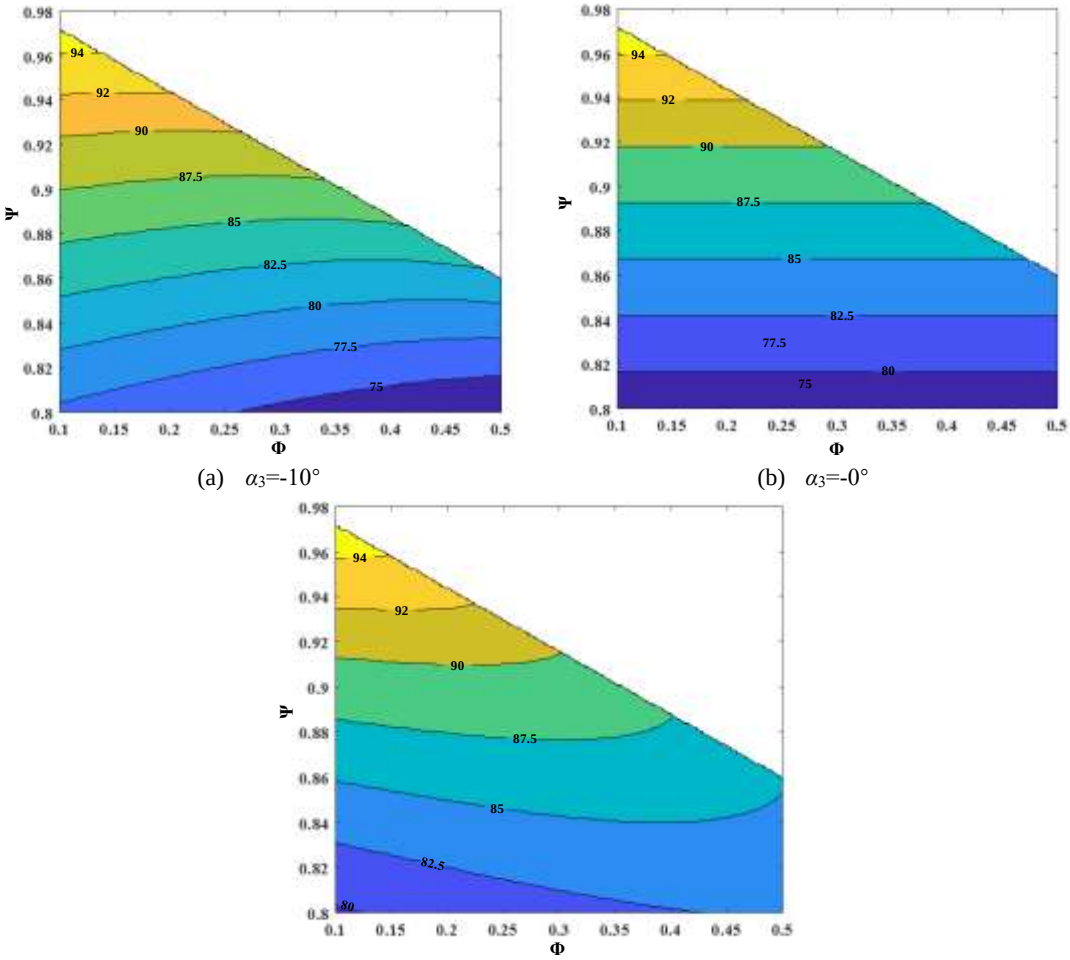

(a) α_3=-10°

(b) α_3=-0°

(c) α_3=10°

Figure 4 Contours of η under various Ψ, Φ and α_3

Based on the dimensionless equations in Table 1, geometrical and flow parameters can be derived, as listed in Table 2. Different from equations in Table 1, equations in Table 2 are dimensional and can be used to determine the shape of the rotor if mass flow rate Q, pressure difference ΔP and thermal properties are given.

Table 2 Equations of geometrical and flow parameters for the liquid turbine

Parameter	Expression	
Radius of the impeller at the inlet of the rotor r_2	$r_2 = \frac{30\sqrt{2}g^{1.5}}{\pi}\frac{\bar{u}}{n_q}\frac{Q^{0.5}}{\Delta p \rho^{0.25}}$	(16)
Height of the blade at the inlet of the rotor h_2	$h_2 = \frac{\tan\beta_2}{120(\Psi-1)\bar{u}^3}\frac{Q^{0.5}}{\Delta p}\frac{n_q}{\rho^{0.25}}$	(17)
Shroud radius at the outlet of the rotor r_{3s}	$r_{3s} = \left(\frac{30\sqrt{2}}{\pi}\bar{D}\bar{u} + \frac{1}{240\bar{D}\bar{u}^2\Phi}\frac{n_q^2}{g^{1.5}}\right)\frac{1}{N}\sqrt{\frac{\Delta p}{\rho}}$	(18)

Hub radius at the outlet of the rotor r_{3h}	$r_{3h}=\left(\frac{30\sqrt{2}}{\pi}\bar{D}\bar{u}-\frac{1}{240\bar{D}\bar{u}^2\Phi}\frac{n_q^2}{g^{1.5}}\right)\frac{1}{N}\sqrt{\frac{\Delta p}{\rho}}$	(19)
Absolute velocity at the inlet of the rotor C_2	$C_2=\bar{u}\sqrt{2\left[\Psi^2+\left(\frac{\Psi-1}{\tan\beta_2}\right)^2\right]\frac{\Delta p}{\rho}}$	(20)
Relative velocity at the inlet of the rotor W_2	$W_2=\bar{u}\sqrt{\frac{2(\Psi-1)}{\sin\beta_2}\frac{\Delta p}{\rho}}$	(21)
Absolute velocity at the outlet of the rotor C_3	$C_3=\frac{\Phi}{\sin\alpha_3}\sqrt{\frac{2\Delta p}{\rho}}$	(22)
Relative velocity at the outlet of the rotor W_3	$W_3=\bar{u}\sigma\sqrt{\frac{2(\Psi-1)}{\sin\beta_2}\frac{\Delta p}{\rho}}$	(23)

3 Preliminary design and model test method

3.1 Preliminary design method

A procedure for designing a liquid turbine is illustrated in Figure 5. Equations for evaluating flow losses are needed to calculate the outlet total pressure. The radius at the inlet of the rotor r_2 is iterated in the design procedure. Geometrical and flow parameters can be derived using equations in Table 2. Design parameters, such as N, Ψ, Φ, β_2 and α_3, need to be adjusted during the design to meet the requirements of the structure and material.

In this paper, the considered flow losses include the incidence loss and the passage loss. The incidence loss can be evaluated using Equation (24), which is derived by Futral and Wasserbauer [56]. The blade angle at the rotor inlet γ_2 is zero and a certain negative incidence angle at the rotor inlet can improve the performance of the rotor for gas turbines.

$$L_i=\frac{1}{2}W_2^2\sin^2\left|\beta_2-\gamma_2\right| \tag{24}$$

There are several correlations for evaluating the passage loss in gas turbines. Although the most accurate formula and coefficients for liquid turbines should be different from those used in gas turbines, the formula proposed by Wasserbauer and Glassman [57] is used in this paper.

$$L_p=\frac{1}{2}K\left(W_2^2\cos^2 i+W_3^2\right) \tag{25}$$

where K is 0.3.

Because the relative flow angle at the rotor exit may not be equal to the blade angle, it causes errors in evaluating the blade loading and the performance of the turbine. However, due to lacking sufficient information, it is hard to correlate the deviation angle for radial inflow turbines [45,58,59]. The ratio of the blade height to the hub radius at the rotor exit of radial inflow turbines can be relatively high compared with axial turbines, so the deviation angle may vary significantly in the radial direction. In addition, due to the secondary flow, the deviation angle also changes in the rotational direction. The complexity of the deviation angle can be illustrated using CFD methods [60]. Thus, in this paper, the mean deviation angle is shown through CFD results.

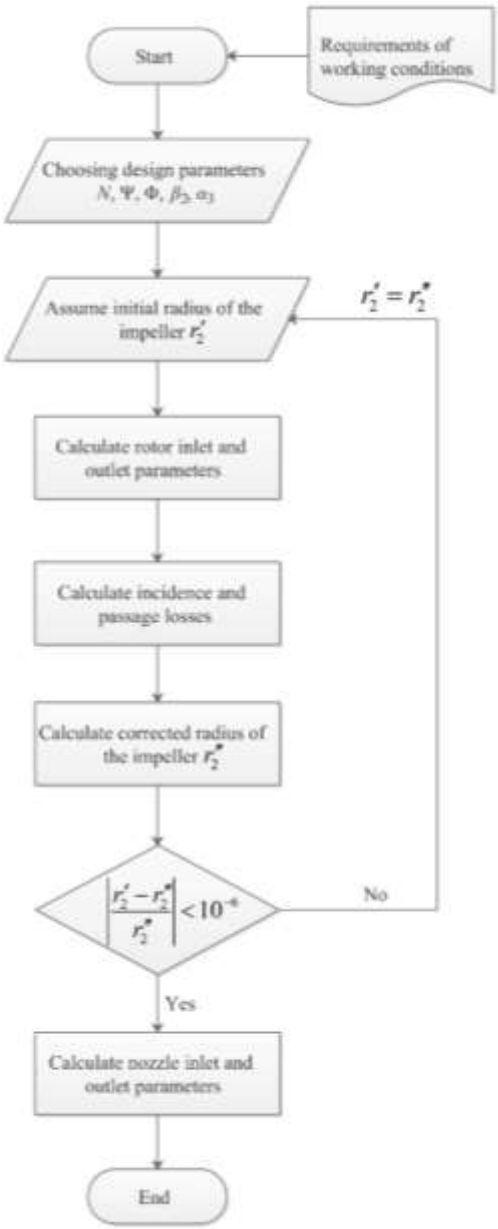

Figure 5 Flow chart of the procedure

Design requirements from SC-CAES are listed in Table 3. The saturation pressure is 0.229 MPa for the isothermal expansion. Flashing in liquid turbines are not permitted in the design method. Therefore, the outflow of the turbine is depressurized further to 0.1 MPa by a throttling valve which is installed downstream the liquid turbine. The flow angle at the outlet of the rotor is zero. The length factor of the rotor is 0.3.

Table 3 Working conditions for the liquid turbine in SC-CAES

Parameters	Value
Fluid	Nitrogen
Inlet total pressure p_0^0	7.0 MPa
Inlet temperature T_0	85 K
Outlet pressure p_3	0.7 MPa
Mass flow rate Q	8.8 kg/s

Based on working conditions in Table 3, design parameters for this study are chosen and listed in Table 4. The deviation of the flow angle between the outlet of the nozzle and the inlet of the rotor is set as 7°, which is validated by numerical results.

Table 4 Selected and derived parameters

Parameters	Value
Load coefficient Ψ	0.90
Flow rate coefficient Φ	0.25
Rotational speed N	25017 rpm
Velocity ratio $\bar{u}$	0.70
Radius ratio $\bar{D}$	0.33
Acceleration factor σ	1.41
Radius at the inlet of the nozzle r_0	45.20 mm
Radius at the outlet of the nozzle r_1	36.51 mm
Radius at the inlet of the rotor r_2	34.77 mm
Shroud radius at the outlet of the rotor r_{3s}	15.03 mm
Hub radius at the outlet of the rotor r_{3h}	8.19 mm
Relative flow angle at the inlet of the rotor β_2	-20.0°
Absolute flow angle at the inlet of the rotor α_2	73.0°
Relative flow angle at the outlet of the rotor β_3	-52.5°
Output power P	63.3 kW
Efficiency η	90.8%

The 3D geometry of the nozzle and the rotor is designed as shown in Figure 6. The profile of the hub and the shroud should be carefully adjusted to make the curvature of these curves smooth. Distributions of meridional passage lines, blade angle, and blade thickness are fitted with Bezier curves. The 3D model of the designed nozzle and the rotor is shown in Figure 6(a). Similar blade shapes are commonly used in radial inflow gas turbines [45]. As show in Figure 6(b), the area of the passage in the nozzle decreases gradually from the inlet to the outlet due to the reflection of the blade and deduction of the radius, while the height of the nozzle blade is constant. Thus, the flow in the nozzle accelerates and the pressure in the nozzle decreases gradually. The area of the passage in the rotor is constant from the 20% streamwise position to the 70% streamwise position. The constant area can help to transfer the thermal energy of the flow into the shaft power while the rotor is rotating, and the flow does not accelerate significantly. As shown in Figure 6(c), the inlet blade angle is zero, so the incidence angle is equal to the negative relative flow angle. This type is beneficial for increasing the strength [61] and reducing the circulation [58]. The radial inflow liquid turbine has a small specific speed because it is commonly used as the turbine for recovering waste energy in industrial systems. The geometry of the liquid turbine is different from that of the hydraulic turbine, because the type of hydraulic turbines is Pelton turbine when the specific speed is small [61].

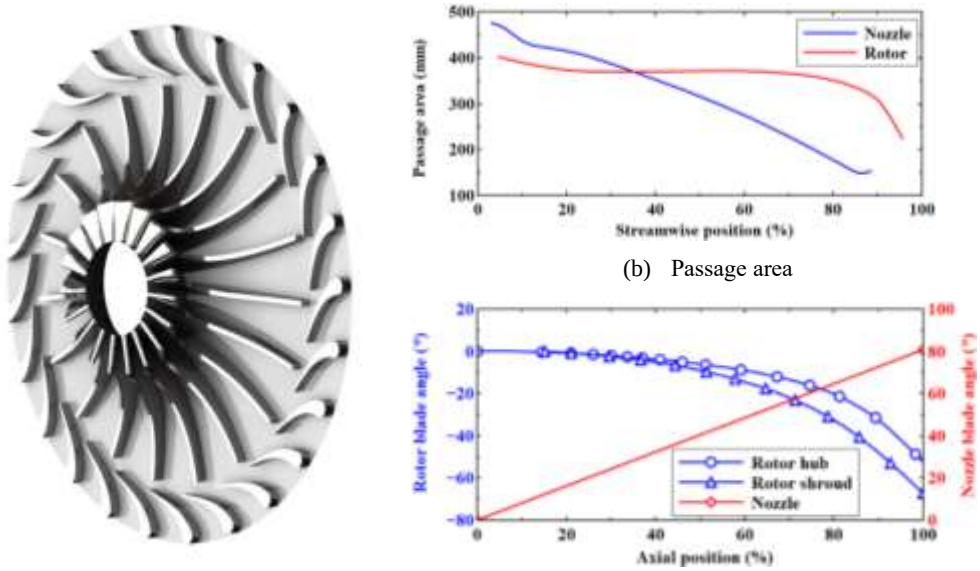

(a) Geometry (b) Passage area (c) Blade angle

Figure 6 3D model of the designed liquid turbine

3.2 Model test method

Due to the limitation of testing, it is hard to construct the corresponding experimental test rig to measure the performance of the designed turbine in the lab. However, model test methods are useful in obtaining the performance of Francis turbines and gas turbines. Dimensionless numbers, for example, Reynold number, are the same among the prototype and the modelled turbine. In addition to dimensionless numbers, principles of the similarities have to be met for pumps and Francis turbines. In this paper, the prototype turbine will be scaled to reduce the rotational speed and increase the diameter of the impeller. In addition, the working fluid is changed from liquid nitrogen to liquid water. Thus, in order to meet the similarity principles, working conditions have to be altered.

The procedure of the model test in this paper consists of two steps, as shown in Figure 7. The prototype turbine is called TA. In the first step, the working fluid is changed from nitrogen to water. The flow rate and the rotational speed is also changed, but the inlet pressure and profiles of the nozzle and the rotor are constant with TA. The turbine at this phase is called TB. In the second step, the geometry of the turbine is reduced, and the inlet pressure and the mass flow rate are also changed. The turbine at this phase is called TC. TC can be tested experimentally on the test rig. In sum, the working fluid is changed from the liquid nitrogen to the water in TB, while the dimension of the turbine is enlarged and the working conditions are also altered in TC.

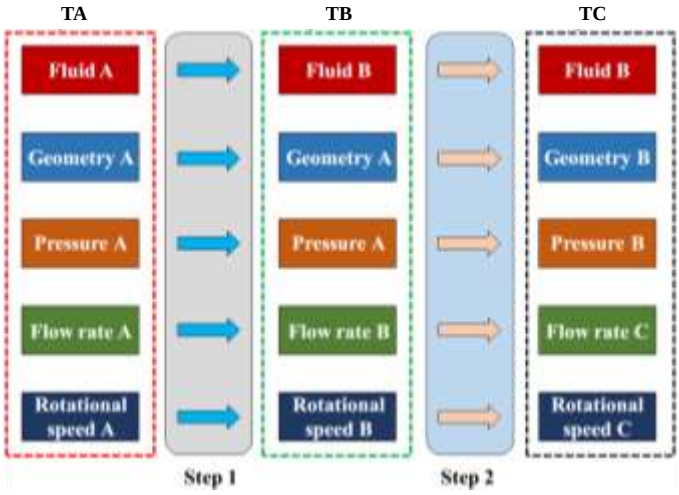

Figure 7 Flow chart of the model test procedure

In the first step, the scale factor δ_a is $\sqrt{\rho^*/\rho}$. If the pressure difference is unchanged with working fluid changed from nitrogen to water, mass flow rate Q_a^* is $Q\delta_a$ and rotational speed N_a^* is N/δ_a. In the second step, the scale factor δ_b is derived by an iteration process based on flow rate similarity, rotation speed similarity and output power similarity. When the pressure difference Δp_b^* is given, the geometry is scaled by δ_b. Both mass flow rate Q_b^* and rotational speed N_b^* are calculated during iteration. It can be found that the model test method in the second step has been used widely for water turbines. In this paper, δ_a is 1.137 and δ_b is 4.441.

4 Experimental and numerical results

4.1 Experimental apparatus

The working conditions needed by the liquid turbine are provided by the test rig. The flow chart is shown in Figure 8(a) and described detailly by Li et al. [30]. The performance of the liquid turbine is measured by pressure sensors (sensors: *a*, *b*, *c* and *d*) at the inlet and outlet of the liquid turbine, a torque sensor (sensor: *e*) on the shaft between the liquid turbine and the electric dynamometer, and a rotational speed sensor (sensor: *f*) at the end of the dynamometer's shaft. The test rig is constructed and shown in Figure 8(b). TC is manufactured and installed in the test section.

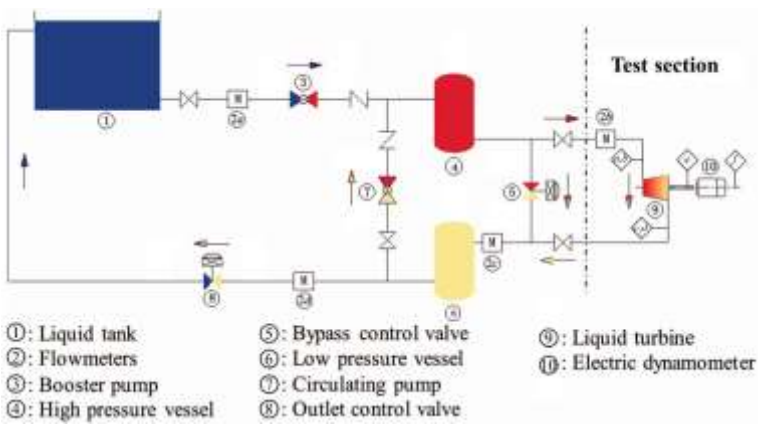

(a) Flow chart

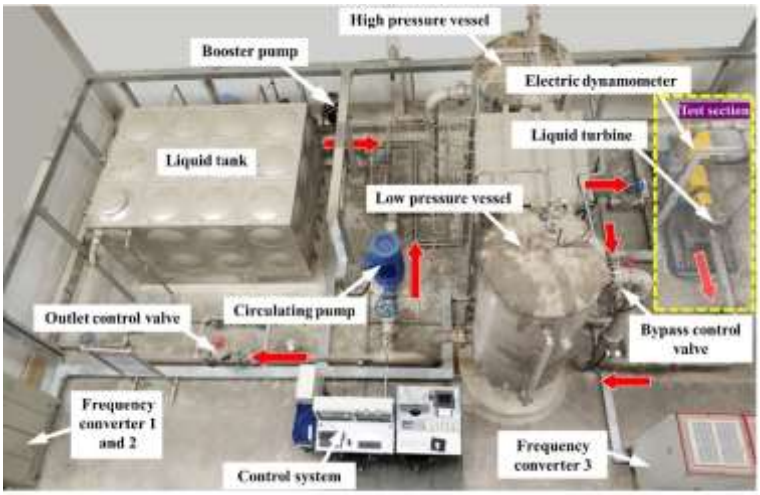

(b) Test rig

Figure 8 Flow chart and test rig [30]

The accuracy of sensors and other devices is listed in Table 5. The largest measurement error is given by the flowmeter and affects both the accuracy of the measured flow rate and turbine efficiency. The measured output power is calculated using the torque sensor (mounted on the shaft between the turbine and the generator) and the rotational speed sensor (mounted on the end of the generator shaft).

Table 5 Accuracy of sensors [48]

Devices	Models	Range	Accuracy
Pressure sensor	STS ATM.IST	0–1.6 MPa	±0.05%
Electromagnetic flowmeter	Krone Optiflux 2100c	0–400 m^3/h	±0.5%
Torque sensor	YB2	0–1000 N·m	±0.5%
Rotational speed sensor	YB2	0–3000 r/min	±1 r/min

The test section is shown in Figure 9(a). The electric dynamometer can convert the shaft power of the turbine to the electric power and control the rotational speed of the turbine using Frequency converter 3. The toque sensor is installed between the liquid turbine and the dynamometer to measure the torque of the turbine's shaft power and calculate the output power of the liquid turbine. The liquid enters the liquid turbine in the vertical direction and flows out of the turbine in the axial direction. The inner view of the manufactured turbine is shown in Figure 9(b). The rotor is assembled at the inner side of the nozzle and its position is adjusted by the nut assembled on the head of the shaft. The position of the nozzle is adjusted by a plate. Ball bearings are used and installed inside the bearing box. The clearance between the shaft and the volute is sealed by the mechanical seal. A cover of the nozzle is assembled on the top surface of the nozzle. There is a clearance between the cover and the shroud of the rotor. Apart of fluid flows through this clearance and produces the leakage loss.

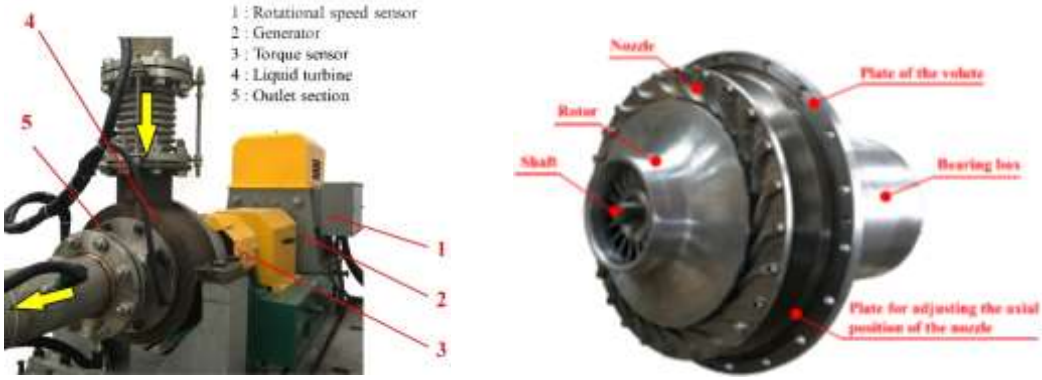

(a) Test section (b) Liquid turbine

Figure 9 Test section and liquid turbine

The volute, nozzle and rotor are shown in Figure 10. The volute is made of 304 stainless steel and its inner side of the volute is a cylinder for convenience in machining, as shown in Figure 10(a). The material of the nozzle is also 304 stainless steel, as shown in Figure 10(b). The material of the rotor is aluminum alloy, and its shroud is melted and fixed on the blades of the rotor through brazing, as shown in Figure 10(c). Detailed performance of the turbine under various working conditions is discussed in the following sections.

(b) Nozzle

(a) Volute (c) Rotor

Figure 10 Components in the liquid turbine [31]

4.2 Numerical simulation

ANSYS CFX is used in the paper to evaluate and compare the performance of TA, TB and TC. However, because the tested turbine consists not only of nozzles and rotor blades but also the volute and clearances, the computational domain includes all flow passages in the tested turbine as shown in Figure 11. The structural mesh of the nozzle and the rotor is constructed by using TurboGrid, as shown in Figure 11(c). The distance between the first layer in the nozzle domain and hub/shroud/blade walls is 0.04 mm, the distance in the rotor domain between the first layer and blade walls is 0.04 mm, and the distance in the rotor domain between the first layer and hub/shroud walls is 0.07 mm. By using ANSYS ICEM, the nonstructural mesh of the volute is constructed as shown in Figure 11(b), while the mesh of Gap B is structural and the mesh of Gap A is unstructured, as shown in Figure 11(d) and (e). Gap B is the chamber between the back of the rotor and the volute. The fluid rotates in Gap B and produces frictional losses. The Gap A is another chamber between

the front of the rotor and the nozzle cover. The fluid in Gap A produces not only frictional losses but also leakage losses.

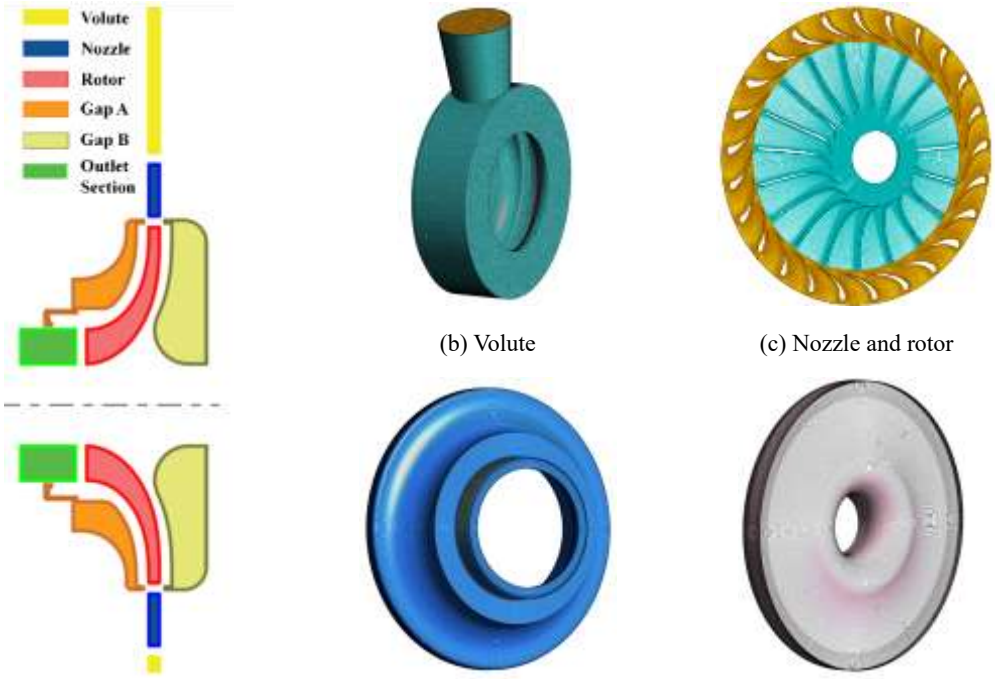

(a) The whole flow passage (b) Volute (c) Nozzle and rotor

(d) Gap A (e) Gap B

Figure 11 Mesh of the flow passage

The amount of elements in the computational domain is listed in Table 6. The turbulence model is k-ε. The inlet boundary condition is mass flow inlet. The outlet boundary condition is the pressure outlet. The rotational speed is set in the rotor domain and on rotating walls in Gap A and Gap B. Values of the boundary conditions are given according to experimental working conditions.

Table 6 The amount of elements in the flow passage (Unit: Million)

Component	Volute	Nozzle	Clearance	Rotor	Gap A	Gap B	Outlet section	Total
Amount	8.3	9.2	0.2	8.9	5.4	4.5	4.0	42.9

4.3 Performance results

The measured and simulated performance of the liquid turbine is illustrated in Figure 12. The experimental flow rate is 61.0 kg/s, the output power is 30.4 kW, and the efficiency is 75.2% at the design working condition. The efficiency of the turbine increases with the flow rate when the working flow rate is lower than the designed flow rate. The output power increases with the flow rate. Detailed analysis of the experimental data can be referred to [30]. The agreement between the experiment and CFD suggests that the numerical simulation is valid to predict the performance of the liquid turbine.

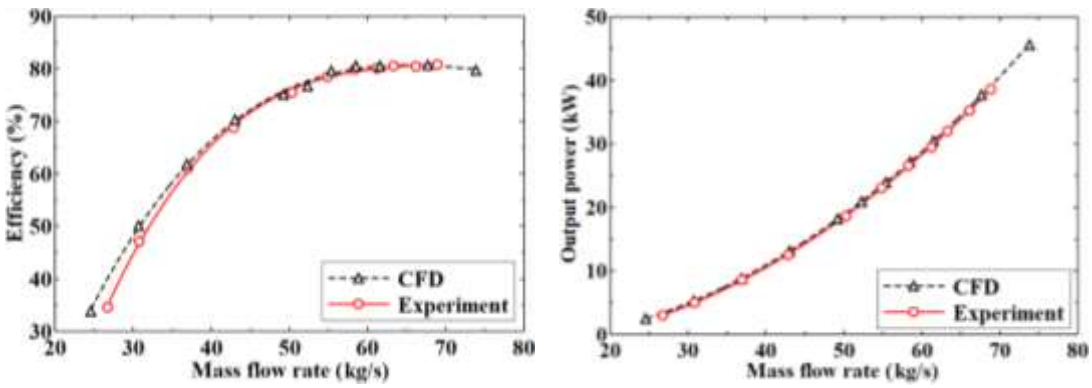

(a) Efficiency (b) Output power

Figure 12 Comparison between the numerical simulation results and the experimental results of TC

In order to compare the performance of the nozzle and the rotor among TA, TB and TC. Using the same numerical methods, predicted performance of TA, TB and TCs' nozzle and rotor can be derived. The total number of elements in the nozzle and the rotor reaches 0.975 million. Working conditions and performance results are compared in Table 7. For TA, the deviation of the output power between design and CFD is 4.4%, and the deviation of the efficiency deviation is 0.0%. For TB, the deviation of the output power is 4.8%, and the deviation of the efficiency is 0.9%. For TC, the deviation of the output power is 4.5%, and the deviation of the efficiency is 2.1%. It is shown that parameters of design agree with CFD in terms of the total performance of turbines because the maximum deviation is less than 5%.

Table 7 Comparison of turbines' performance between the design and CFD

Parameters	TA		TB		TC	
Fluid	Nitrogen		Water		Water	
Density	771 kg/m^3		997 kg/m^3		997 kg/m^3	
Mass flow rate	8.8 kg/s		10.0 kg/s		61.5 kg/s	
Rotational speed	25,017 rpm		22,000 rpm		1,550 rpm	
	Design	Simulation	Design	Simulation	Design	Simulation
Output power	63.3 kW	60.5 kW	55.7 kW	53.0 kW	33.1 kW	31.6 kW
Efficiency	90.8%	90.8 %	90.8 %	90.0%	90.8%	88.9%
Nozzle inlet total pressure	7.0 MPa	6.8 MPa	7.0 MPa	6.8 MPa	1.3 MPa	1,3 MPa
Rotor inlet pressure	4.0 MPa	3.9 MPa	4.0 MPa	4.0 MPa	-	1.0 MPa
Rotor outlet pressure	0.7 MPa	0.7 MPa	0.7 MPa	0.7 MPa	0.7 MPa	0.7 MPa

Contours of pressure coefficient are shown in Figure 13. The pressure decreases gradually from the inlet to the outlet through flow passages. From the inlet of the nozzle to and middle of the rotor, the contours are in the direction of quasi-orthogonal lines. Because the contours of the pressure coefficient are similar among TA, TB and TC, it indicates that the flow in the modelled turbines (TB and TC) using the model test method is similar to the prototype turbine (TA).

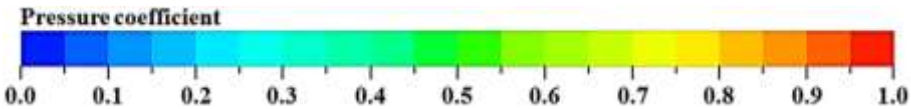

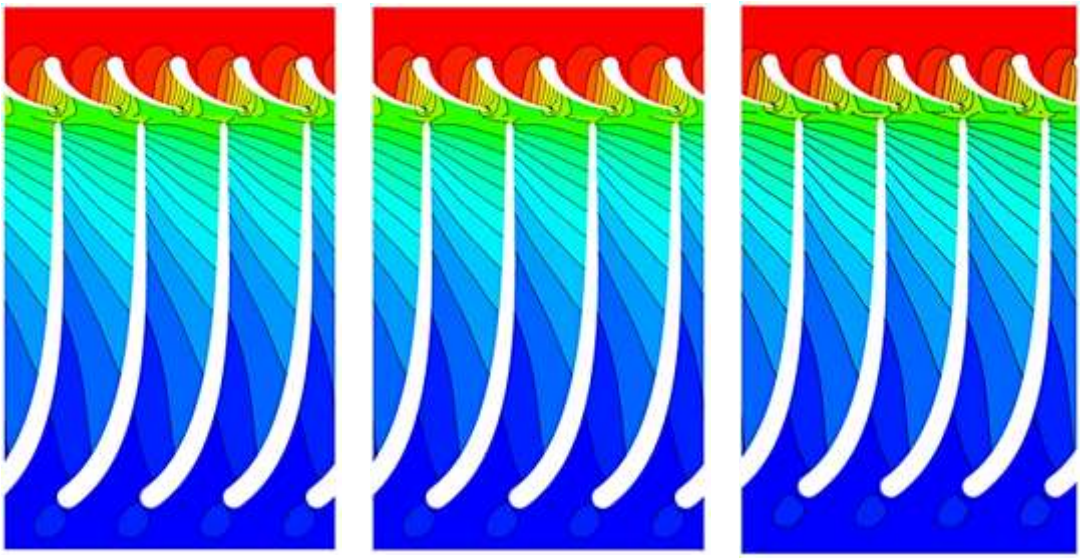

(a) TA (b) TB (c) TC

Figure 13 Contours of pressure coefficient on the mid-span blade to blade plane

For various working conditions, the predicted performance of design, TA, TB and TC is illustrated in Figure 14. Computational domains in Figure 14 only include the nozzle and the rotor, so the design performance can be compared with simulation results, which are derived using the same method in Figure 12. As shown in Figure 14(a), the efficiency of TA, TB and TC is lower than the design in the entire range of flow rate. Among TA, TB and TC, the efficiency of TA is the closest to the design and the deviation between TA and the design is less than 2% in the entire range of the flow rate. The deviation of the efficiency between TB and the design decreases as the flow rate increases if the flow rate is lower than 80% and increases with the flow rate if the flow rate is higher than 80%. The variation trend of the deviation between TC and the design is consistent with that between TB and the design. It should be noted that the deviation of efficiency between TB and TC is closest when the flow rate is 50%. Figure 14(b) shows the normalization of the efficiency can reflect the trend of the efficiency and is defined as $(\eta - \eta_{min})/(\eta_{max} - \eta_{min})$. In the entire range of the flow rate, the variation of the normalized efficiency is similar among the design, TA, TB and TC. The normalized efficiency of TB and TC is higher than that of the design if the flow rate is between 60% and 90%, but the normalized efficiency of the TA is a little higher than the design if the flow rate is 60% and lower than the design if the flow rate is between 70% and 100%. In Figure 14(c), the output power increases with the flow rate. TA's output power is higher than the design and the deviation between TA and the design increases with the flow rate. TB's output power is lower than the design and the deviation between TB and the design is almost constant within the entire range of the flow rate. Due to the model testing, the output power of TC is lower than the output power of the design, TA and TC. However, as shown in Figure 14(d), the normalized output power of TC agrees with the design, TA and TB.

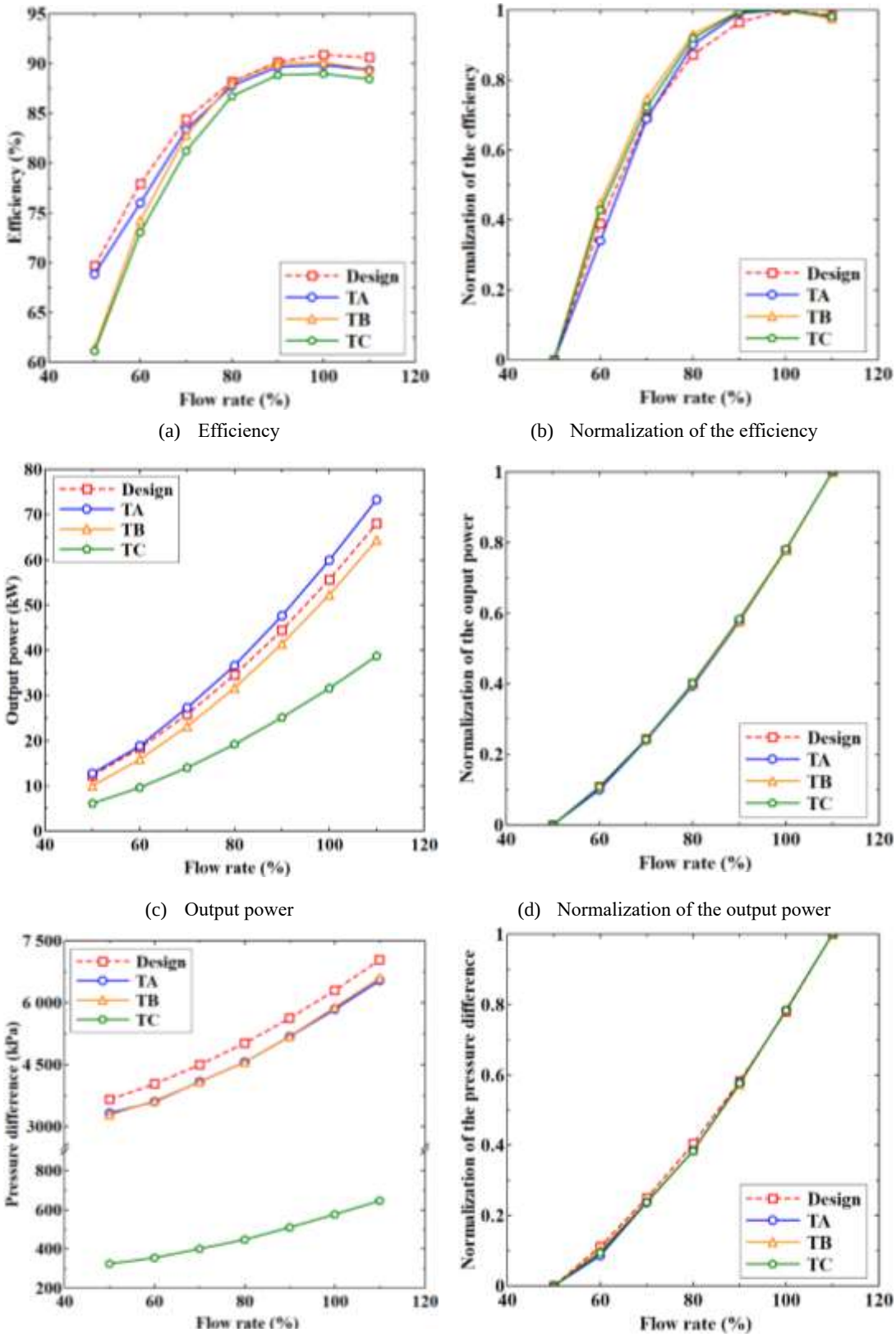

(a) Efficiency (b) Normalization of the efficiency

(c) Output power (d) Normalization of the output power

(e) Pressure difference (f) Normalization of the pressure difference

Figure 14 Comparison of turbines' performance under various flow rates between the design and CFD

In Figure 14(e), the pressure difference is defined as the pressure reduction between the inlet of the nozzle and the outlet of the rotor. The pressure difference increases with the flow rate. There is a constant deviation between the design and TA and TB within the entire flow rate range. The

deviation of the pressure difference indicates that the predicted flow loss in the design is lower than that in TA and TB. TC's pressure difference is much lower than the pressure difference of the design, TA and TB due to the model testing. In Figure 14(f), the normalized pressure difference of TC agrees with the design, TA and TB.

5 Discussions

Reasonable ranges of geometrical and flow parameters for liquid turbines are different from those of gas turbines because the thermal properties of the liquid are different from the steam and the gas. The height of the blade at the inlet of the rotor h_2 and the hub radius of the rotor r_{3h} should not be too small due to the requirements from the structure, the strength and the flow. The area ratio $\bar{A}$ should be in the appropriate range to reduce the flow loss in the rotor. The three parameters are dependent and related to many other parameters. Each of them cannot be determined by one criterion.

5.1 The blade height at the rotor inlet

The height ratio $\bar{h}_2$ can be evaluated using Equation (13), as shown in Figure 15(a). The reasonable range for $\bar{h}_2$ is 0.04~0.32 for gas turbines. When β_2 is larger than -10°, it is hard to adjust Ψ and $\bar{u}$ o make $\bar{h}_2$ in the reasonable range. Ψ should be large enough, and $\bar{u}$ has to be reduced to a sufficiently low value. When β_2 is lower than -10°, it will be much easier to choose Ψ and $\bar{u}$. Thus, large inlet flow angle is beneficial to select Ψ and $\bar{u}$ to make $\bar{h}_2$ large enough.

The inlet rotor height is determined by $\bar{h}_2$ and working conditions. h_2 could be derived as

$$h_2 = \frac{\tan\beta_2}{120(\Psi-1)\bar{u}^2}\left(\frac{Q^2}{g\Delta p}\right)^{\frac{1}{4}} g n_q \tag{26}$$

Using the working conditions given in Table 3, the height of the blade h_2 is calculated, as shown in Figure 15. For structure reasons, h_2 should not be too small. In Figure 15(b), n_q is equal to 5. When $\bar{u}$ is 0.5, Ψ is 0.85, and β_2 is -10°, h_2 is equal to 0.394 mm. The height decreases as $\bar{u}$ increases if other geometry parameters are unchanged. In Figure 15(c), n_q is equal to 30. When $\bar{u}$ is 0.7, Ψ is 0.85, and β_2 is -10°, h_2 is 1.207 mm. When β_2 is -20°, h_2 is 2.490 mm.

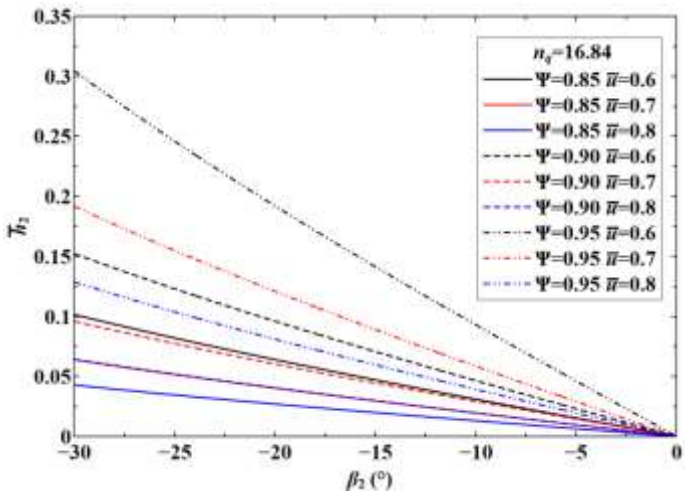

(a) Rotor inlet height ratio varied with β_2, Ψ, $\bar{u}$

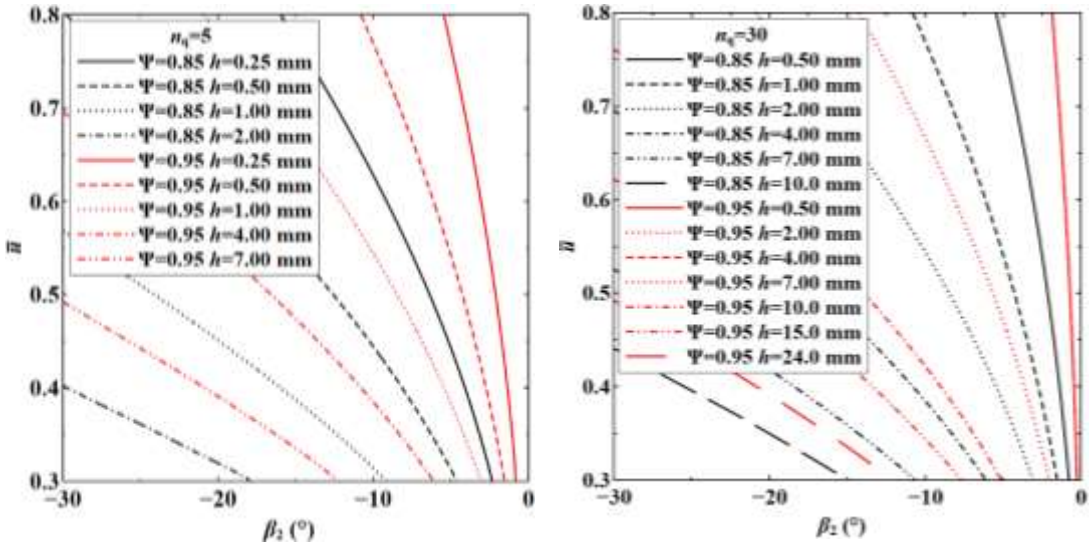

(b) Rotor inlet height at n_q=5 (c) Rotor inlet height at n_q=5

Figure 15 Rotor inlet blade height and height ratio

5.2 The hub radius at the rotor outlet

Using mass conservation and geometry relationship, r_{3h} is derived as

$$r_{3h} = \left(\frac{30\sqrt{2}}{\pi} \frac{\bar{u}\bar{D}}{n_q} - \frac{1}{240g^{1.5}} \frac{n_q^2}{\bar{u}^2 \Phi \bar{D}} \right) \left(\frac{Q^2}{\rho \Delta p} \right)^{\frac{1}{4}} \tag{27}$$

If r_{3h} is not large enough, there is not sufficient space near the hub to install the blades, and the flow near the root of the blade may be choked. The relationship in Equation (27) can be illustrated in Figure 17. Although there is a peak value for r_{3h} according to Equation (27), r_{3h} increases as $\bar{D}$ and $\bar{u}$ increases, and Φ and n_q decrease within the range in Figure 16. When Φ is 0.29, $\bar{D}$ is 0.3, n_q is 5, and n_q is 0.5, r_{3h} is 23.104 mm. When $\bar{u}$ is 0.8, r_{3h} is 39.297 mm as shown in Figure 16(a). When n_q is equal to 30, r_{3h} is 2.159 mm as shown in Figure 16(b).

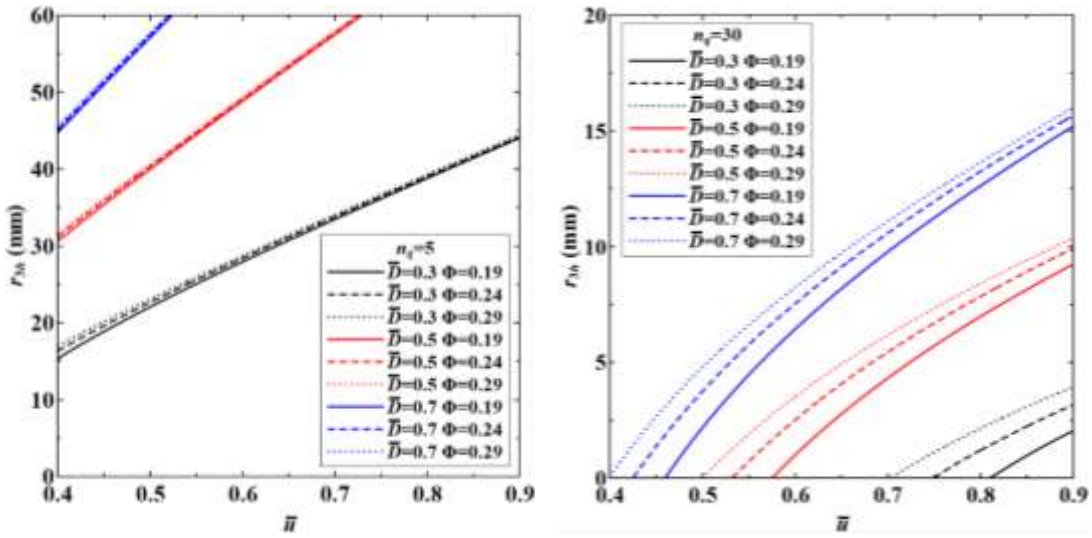

(a) n_q=5 (b) n_q=30

Figure 16 Rotor inlet blade hub radius

5.3 The area ratio

There is a strong connection between the slip ratio σ and the area ratio $\bar{A}$ as derived in Equation (28). Because the slip ratio σ affects the flow separation and the viscous losses in the flow

passage, $\bar{A}$ should be carefully chosen.

$$\sigma = \frac{\cos\beta_2}{\bar{A}\cos\beta_3} \tag{28}$$

The relationship in Equation (28) can be illustrated in Figure 18. When σ is between 1 and 1.5 and β_3 is lower than -55°, $\bar{A}$ should be set between 1 and 2. Compared to β_2, β_3 affects more significantly as shown in Figure 17.

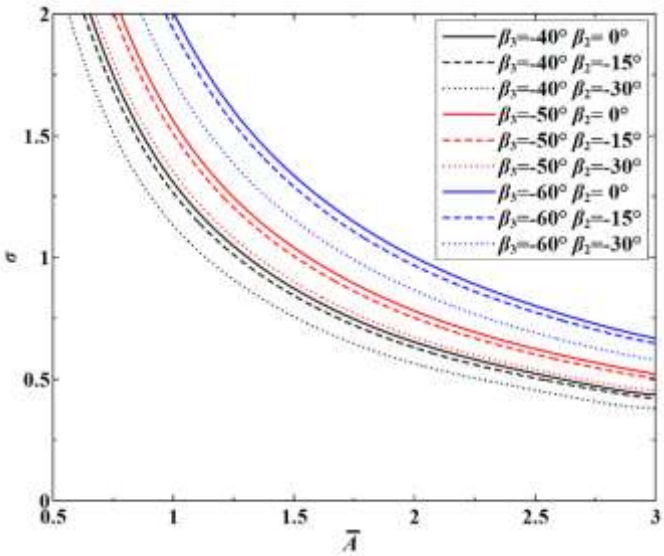

Figure 17 The acceleration ratio σ varied with $\bar{A}$, β_2 and β_3

Using mass conversation, $\bar{A}$ can read as

$$\bar{A} = \frac{\Psi - 1}{\Phi \tan\beta_2} \tag{29}$$

Figure 18(a) illustrates the relationship of parameters in Equation (29). The loading coefficient affects Ψ more remarkably than $\bar{A}$. If the inlet rotor relative flow angle β_2 is less than -10°, it will be hard to choose appropriate set of parameters to make the area ratio within the reasonable range. Using the geometrical relationship, $\bar{A}$ is also equal to $\bar{D}\bar{h}$, as shown in Figure 18(b).

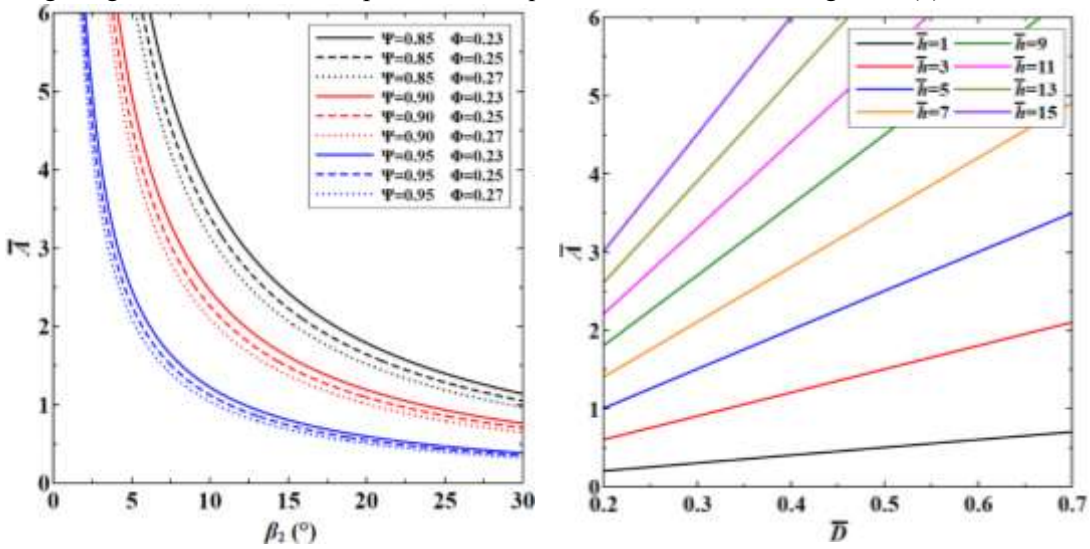

(a) $\bar{A}$ varied with β_2, Φ, Ψ (b) $\bar{A}$ varied with $\bar{D}$ and $\bar{h}$

Figure 18 Relationship between $\bar{A}$ and other parameters

6 Conclusion

This paper proposed a preliminary design and model test method of the liquid turbine used in SC-CAES systems. Relationships of geometry and flow parameters are derived, and the performance of the liquid turbine is evaluated.

The efficiency of the designed liquid turbine is 92%, the power is 65.7 kW, and the rotational speed is 25,017 rpm. Performance of two other turbines derived by model test methods is studied using CFD methods which are validated by experimental results. It indicates that the design performance can agree with that of model turbines near the design working condition, while there is a certain deviation when the flow rate is less than 70%.

The relationship between geometrical and flow parameters are discussed. Appropriate ranges of design parameters are different from gas turbines due to the deviation of thermal properties between the liquid and the gas. Design parameters will be optimized and considerations about correlations of exit deviations and pressure losses in future research.

Acknowledgement

This research is supported by the National Science Fund for Distinguished Young Scholars No. 51925604, International Partnership Program, Bureau of International Cooperation of Chinese Academy of Sciences No. 182211KYSB20170029, Guizhou Province Large Scale Physical Energy Storage Technology Research and Development Platform No. [2019]4011.

Nomenclature

Variables

A	Passage area, m^2
$\bar{A}$	Passage ratio
C	Absolute velocity, m/s
$\bar{D}$	Rotor radius ratio
h	Blade height, m
$\bar{h}$	Blade height ratio
g	Acceleration of gravity, m/s^2
i	Incidence angle, °
I	Enthalpy, J
K	Empirical coefficient
l	Flow path length, m
L	Energy of loss, J
m	Mass flow rate, kg/s
n_q	Specific rotational speed
N	Rotational speed, rpm
p	Pressure, MPa
r	Radius, m
T	Temperature, K
U	Blade peripheral speed, m/s
$\bar{u}$	Speed ratio

P	Output power, kW
X	Parameter set at any computational location
y	Blade loading ratio
Y	Blade loading, J
W	Relative velocity, m/s
Z	Axial locations, m
Z_h	Height location, m

Greek symbols

α	Absolute flow angle, °
β	Relative flow angle, °
δ	Scale factor
η	Efficiency, %
θ	Circumferential angle, °
Θ	Radius ratio distribution
ξ	Pressure coefficient distribution
ρ	Density, kg/m^3
σ	Acceleration factor
τ	Relative velocity ratio distribution
Φ	Flow rate coefficient
χ	Distribution of relative velocity ratio between the real flow and isentropic flow
Ψ	Loading coefficient
Ω	Reaction degree

Subcripts

0	Nozzle inlet
1	Nozzle outlet
2	Rotor inlet
3	Rotor outlet
a	The first step of the model test procedure
b	The second step of the model test procedure
g	Gas
h	Hub
i	Incidence
j	Computational station
m	Streamwise location
N	Nozzle
p	Passage
r	Radial direction
R	Rotor
s	Shroud
ts	Total to static
tt	Total to total
u	Circumferential direction

Supercripts

0	Total state
*	Modeled parameter

Author Contributions

H.L. mainly contributes in the methodology, investigation, experiment, CFD, flow analysis and original draft preparation; Z.S. mainly contributes in the experiment; X.Z. mainly contributes in the methodology and experiment; Y.Z. mainly contributes in the methodology; W.L. mainly contributes in the methodology, experiment, flow analysis and draft review and editing; H.C. mainly contributes in the draft review and editing, project administration and funding acquisition; Z.Y. mainly contributes in the flow analysis and draft review. All authors have read and agreed to the published version of the manuscript.

Conflicts of Interest

The authors declare that they have no known competing financial interests or personal relationships that could have appeared to influence the work reported in this paper.

References

[1] H. Li, W. Li, X. Zhang, Y. Zhu, H. Chen, Research progress of liquid expanders, J. Eng. Thermophys. 40 (2019) 1041–1049.

[2] H. Guo, Y. Xu, H. Chen, X. Zhou, Thermodynamic characteristics of a novel supercritical compressed air energy storage system, Energy Convers. Manag. 115 (2016) 167–177. https://doi.org/10.1016/j.enconman.2016.01.051.

[3] H. Chen, C. Tan, J. Liu, Y. Xu, Z. Yang, Energy storage system using supercritical air, WO2011/054169, 2010.

[4] H. Guo, Y. Xu, H. Chen, C. Guo, W. Qin, Thermodynamic analytical solution and exergy analysis for supercritical compressed air energy storage system, Appl. Energy. 199 (2017) 96–106. https://doi.org/10.1016/j.apenergy.2017.04.068.

[5] Huan Guo, Performance study on novel compressed air energy storage systems, 2013.

[6] Z. Zhang, Y. Ma, M. Li, L. Zhao, Recent advances of energy recovery expanders in the transcritical CO2 refrigeration cycle, HVAC&R Res. 19 (2013) 376–384. https://doi.org/10.1080/10789669.2013.784644.

[7] A.A. Murthy, A. Subiantoro, S. Norris, M. Fukuta, A review on expanders and their performance in vapour compression refrigeration systems, Int. J. Refrig. 106 (2019) 427–446. https://doi.org/10.1016/j.ijrefrig.2019.06.019.

[8] H. Taniguchi, K. Kudo, W.H. Giedt, I. Park, S. Kumazawa, Analytical and experimental investigation of two-phase flow screw expanders for power generation, J. Eng. Gas Turbines Power. 110 (1988) 628–635. https://doi.org/10.1115/1.3240182.

[9] B.P. Kliem, Fundamentals of the two-phase screw-type engine, Dissertation, Fakultät für Maschinenbau, Universität Dortmund, 2015.

[10] I.K. Smith, N. Stosic, C.A. Aldis, Lysholm machines as two-phase expanders, in: Proc. 1994 Int. Compress. Eng. Conf. Purdue, West Lafayette, IN, US, 1994: p. 957.

[11] H. Öhman, P. Lundqvist, Experimental investigation of a Lysholm turbine operating with superheated, saturated and 2-phase inlet conditions, Appl. Therm. Eng. 50 (2013) 1211–1218. https://doi.org/10.1016/j.applthermaleng.2012.08.035.

[12] H. Vasuthevan, A. Brümmer, Theoretical investigation of flash vaporisation in a screw expander, IOP Conf. Ser. Mater. Sci. Eng. 232 (2017) 12077. https://doi.org/10.1088/1757-899x/232/1/012077.

[13] G. Bianchi, S. Kennedy, O. Zaher, S.A. Tassou, J. Miller, H. Jouhara, Numerical modeling of a two-phase twin-screw expander for Trilateral Flash Cycle applications, Int. J. Refrig. 88 (2018) 248–259. https://doi.org/10.1016/j.ijrefrig.2018.02.001.

[14] M. Kakuda, H. Nagata, F. Ishizono, Development of a scroll expander for the CO2 refrigeration cycle, HVAC&R Res. 15 (2009) 771–783. https://doi.org/10.1080/10789669.2009.10390863.

[15] H. Wang, R.B. Peterson, T. Herron, Experimental performance of a compliant scroll expander for an organic Rankine cycle, Proc. Inst. Mech. Eng. Part A J. Power Energy. 223 (2009) 863–872. https://doi.org/10.1243/09576509JPE741.

[16] C. Xia, W. Zhang, G. Bu, Z. Wang, P. Shu, Experimental study on a sliding vane expander in the HFC410A refrigeration system for energy recovery, Appl. Therm. Eng. 59 (2013) 559–567. https://doi.org/10.1016/j.applthermaleng.2013.05.050.

[17] G. Ferrara, L. Ferrari, D. Fiaschi, G. Galoppi, S. Karellas, R. Secchi, D. Tempesti, Energy recovery by means of a radial piston expander in a CO2 refrigeration system, Int. J. Refrig. 72 (2016) 147–155. https://doi.org/10.1016/j.ijrefrig.2016.07.014.

[18] G. Galoppi, R. Secchi, L. Ferrari, G. Ferrara, S. Karellas, D. Fiaschi, Radial piston expander as a throttling valve in a heat pump: Focus on the 2-phase expansion, Int. J. Refrig. 82 (2017) 273–282. https://doi.org/10.1016/j.ijrefrig.2017.06.025.

[19] J. Nickl, G. Will, H. Quack, W.E. Kraus, Integration of a three-stage expander into a CO2 refrigeration system, Int. J. Refrig. 28 (2005) 1219–1224. https://doi.org/10.1016/j.ijrefrig.2005.08.012.

[20] W.J. Comfort III, C.W. Beadle, Design considerations for a two-phase turbine, in: Symp. Polyph. Flow Turbomachinery, ASME Winter Annu. Meet., San Francisco, California, 1978.

[21] K. Wang, J. Sun, P. Song, Experimental study of cryogenic liquid turbine expander with closed-loop liquefied nitrogen system, Cryogenics (Guildf). 67 (2015) 4–14. https://doi.org/10.1016/j.cryogenics.2015.01.004.

[22] K. Li, J. Sun, J. Fu, P. Song, Design and numerical flow analysis of a LNG power recovery turbine, in: Proc. ASME Turbo Expo 2013 Turbine Tech. Conf. Expo. Vol. 5B Oil Gas Appl. Steam Turbines, San Antonio, Texas, USA, 2013. https://doi.org/10.1115/GT2013-94900.

[23] P. Song, J. Sun, K. Wang, Swirling and cavitating flow suppression in a cryogenic liquid turbine expander through geometric optimization, Proc. Inst. Mech. Eng. Part A J. Power Energy. 229 (2015) 628–646. https://doi.org/10.1177/0957650915589062.

[24] P. Song, J. Sun, C. Huo, Cavitating flow suppression for a two-phase liquefied natural gas expander through collaborative fine-turning design optimization of impeller and exducer geometric shape, J. Fluids Eng. 142 (2020) 051401. https://doi.org/10.1115/1.4045713.

[25] Z. He, Y. Ge, J. Sun, K. Wang, Numerical study of cavitating behavior in a cryogenic liquid

turbine, in: Proc. ASME Turbo Expo 2012 Turbine Tech. Conf. Expo. Vol. 8 Turbomachinery, Parts A, B, C, Copenhagen, Denmark, 2012: pp. 2581–2592. https://doi.org/10.1115/GT2012-68774.

[26] S. Sun, J. Sun, W. Sun, P. Song, Enhancing cryogenic cavitation prediction through incorporating modified cavitation and turbulence models, J. Fluids Eng. 143 (2021) 061404. https://doi.org/10.1115/1.4050056.

[27] Y. Ren, J. Sun, R. Zheng, P. Song, K. Wang, Investigation of impeller strength for a cryogenic liquid turbine, in: Proc. ASME Turbo Expo 2010 Power Land, Sea, Air. Vol. 6 Struct. Dyn. Parts A B, Glasgow, UK, 2010: pp. 1333–1343. https://doi.org/10.1115/GT2010-23125.

[28] K. Wang, J. Sun, Z. He, P. Song, Prediction of axial thrust load acting on a cryogenic liquid turbine impeller, in: Proc. ASME 2011 Turbo Expo Turbine Tech. Conf. Expo. Vol. 6 Struct. Dyn. Parts A B, Vancouver, British Columbia, Canada, 2011: pp. 487–498. https://doi.org/10.1115/GT2011-45273.

[29] P. Song, J. Sun, K. Wang, Z. He, Development of an optimization design method for turbomachinery by incorporating the cooperative coevolution genetic algorithm and adaptive approximate model, in: Proc. ASME 2011 Turbo Expo Turbine Tech. Conf. Expo. Vol. 7 Turbomachinery, Parts A, B, C, Vancouver, British Columbia, Canada, 2011: pp. 1139–1153. https://doi.org/10.1115/GT2011-45411.

[30] H. Li, X. Zhang, W. Li, Y. Zhu, Z. Zuo, H. Chen, Experimental investigation of a liquid turbine in a full performance test rig, Proc. Inst. Mech. Eng. Part A J. Power Energy. 233 (2018) 337–345. https://doi.org/10.1177/0957650918785793.

[31] H. Li, Experimental and numerical invesitgation of liquid expanders, University of Chinese Academy of Sciences, 2018.

[32] S. Sgambati, F. Haensel, Cryogenic liquid expansion turbine, WO2013057561A1, 2011.

[33] S.L. Dixon, C.A. Hall, Chapter 8 - Radial-flow gas turbines, in: S.L. Dixon, C.A.B.T.-F.M. and T. of T. (Seventh E. Hall (Eds.), Butterworth-Heinemann, Boston, 2014: pp. 319–360. https://doi.org/10.1016/B978-0-12-415954-9.00008-5.

[34] C. Rodgers, Review of mixed flow and radial turbine options, in: 26th Jt. Propuls. Conf., American Institute of Aeronautics and Astronautics, 1990: p. AIAA 1990-2414. https://doi.org/doi:10.2514/6.1990-2414.

[35] A.J. Feneley, A. Pesiridis, A.M. Andwari, Variable geometry turbocharger technologies for exhaust energy recovery and boosting-a review, Renew. Sustain. Energy Rev. 71 (2017) 959–975. https://doi.org/10.1016/j.rser.2016.12.125.

[36] D. Kim, Y. Kim, Preliminary design and performance analysis of a radial inflow turbine for organic Rankine cycles, Appl. Therm. Eng. 120 (2017) 549–559. https://doi.org/10.1016/j.applthermaleng.2017.04.020.

[37] V. Mounier, L.E. Olmedo, J. Schiffmann, Small scale radial inflow turbine performance and pre-design maps for Organic Rankine Cycles, Energy. 143 (2018) 1072–1084. https://doi.org/10.1016/j.energy.2017.11.002.

[38] D. Fiaschi, G. Manfrida, F. Maraschiello, Design and performance prediction of radial ORC turboexpanders, Appl. Energy. 138 (2015) 517–532. https://doi.org/10.1016/j.apenergy.2014.10.052.

[39] J. Qi, T. Reddell, K. Qin, K. Hooman, I.H.J. Jahn, Supercritical CO2 radial turbine design performance as a function of turbine size parameters, J. Turbomach. 139 (2017) 081008.

https://doi.org/10.1115/1.4035920.
[40] K.G. Nithesh, D. Chatterjee, C. Oh, Y.-H. Lee, Design and performance analysis of radial-inflow turboexpander for OTEC application, Renew. Energy. 85 (2016) 834–843. https://doi.org/10.1016/j.renene.2015.07.018.
[41] Z. Krzemianowski, J. Steller, High specific speed Francis turbine for small hydro purposes-Design methodology based on solving the inverse problem in fluid mechanics and the cavitation test experience, Renew. Energy. 169 (2021) 1210–1228. https://doi.org/10.1016/j.renene.2021.01.095.
[42] A. Whitfield, N.C. Baines, Design of radial turbomachines, Longman Scientific & Technical, 1990.
[43] D.G. Wilson, T. Korakianitis, The design of high-efficiency turbomachinery and gas turbines, Second, MIT Pres, Cambridge, Massachusetts, 2014.
[44] A. Whitfield, The preliminary design of radial inflow turbines, J. Turbomach. 112 (1990) 50–57. https://doi.org/10.1115/1.2927420.
[45] H. Moustapha, M.F. Zelesky, N.C. Balnes, D. Japikse, Axial and radial turbines, Concepts NREC, Vermont, US, 2003.
[46] Y.S. Li, G.L. Lu, Radial-inflow turbine and centrifugal compressor, China Machine Press, Beijing, 1987.
[47] X. Zhang, Multistage radial turbine for supercritical air energy storage system, Institute of Engineering Thermophysics, Chinese Academy of Sciences, 2014.
[48] N. Ansarifard, S.S. Kianejad, A. Fleming, S. Chai, A radial inflow air turbine design for a vented oscillating water column, Energy. 166 (2019) 380–391. https://doi.org/10.1016/j.energy.2018.10.068.
[49] Z. Han, X. Jia, P. Li, Preliminary design of radial inflow turbine and working fluid selection based on particle swarm optimization, Energy Convers. Manag. 199 (2019) 111933. https://doi.org/10.1016/j.enconman.2019.111933.
[50] Y. Zheng, D. Hu, Y. Cao, Y. Dai, Preliminary design and off-design performance analysis of an Organic Rankine Cycle radial-inflow turbine based on mathematic method and CFD method, Appl. Therm. Eng. 112 (2017) 25–37. https://doi.org/10.1016/j.applthermaleng.2016.10.036.
[51] D. Fiaschi, G. Manfrida, F. Maraschiello, Thermo-fluid dynamics preliminary design of turbo-expanders for ORC cycles, Appl. Energy. 97 (2012) 601–608. https://doi.org/10.1016/j.apenergy.2012.02.033.
[52] K. Zhou, J. Wang, J. Xia, Y. Guo, P. Zhao, Y. Dai, Design and performance analysis of a supercritical CO2 radial inflow turbine, Appl. Therm. Eng. 167 (2020) 114757. https://doi.org/10.1016/j.applthermaleng.2019.114757.
[53] S. Lee, H. Gurgenci, A comparison of three methodological approaches for meanline design of supercritical CO2 radial inflow turbines, Energy Convers. Manag. 206 (2020) 112500. https://doi.org/10.1016/j.enconman.2020.112500.
[54] H. Li, S. Rane, Z. Yu, G. Yu, An inverse mean-line design method for optimizing radial outflow two-phase turbines in geothermal systems, Renew. Energy. 168 (2021) 463–490. https://doi.org/10.1016/j.renene.2020.12.079.
[55] H. Li, S. Rane, Z. Yu, Investigation of the performance and flow characteristics of two-phase reaction turbines in total flow geothermal systems, Renew. Energy. 175 (2021) 345–372.

https://doi.org/10.1016/j.renene.2021.05.022.

[56] S.M. Futral, Off-design performance prediction with experimental verification for a radial-inflow turbine: Samuel M. Futral Jr. and Charles A. Wasserbauer, National Aeronautics and Space Administration, Cleveland, Ohio, US, 1965.

[57] C.A. Wasserbauer, A.J. Glassman, FORTRAN program for predicting off-design performance of radial-inflow turbines, Cleveland, Ohio, US, 1975.

[58] D. Japikse, N.C. Baines, Introduction to turbomachinery, Concepts ETI, Inc. and Oxford University Press, Vermont, US and Oxford, UK, 1994.

[59] A. Meroni, M. Robertson, R. Martinez-Botas, F. Haglind, A methodology for the preliminary design and performance prediction of high-pressure ratio radial-inflow turbines, Energy. 164 (2018) 1062–1078. https://doi.org/10.1016/j.energy.2018.09.045.

[60] K. Otsuka, T. Komatsu, H. Tsujita, S. Yamaguchi, A. Yamagata, Numerical analysis of flow in radial turbine (Effects of nozzle vane angle on internal flow), Int. J. Fluid Mach. Syst. 9 (2016) 137–142. https://doi.org/10.5293/ijfms.2016.9.2.137.

[61] S.L. Dixon, C. Hall, Fluid mechanics and thermodynamics of turbomachinery, Butterworth-Heinemann, 2014. https://doi.org/10.1016/C2011-0-05059-7.